# Localized Changes of Stainless Steel Powder Characteristics During Selective Laser Melting Additive Manufacturing

D. GALICKI, F. LIST, S.S. BABU, A. PLOTKOWSKI, H.M. MEYER III, R. SEALS, and C. HAYES

In laser powder bed additive manufacturing processes, feedstock materials are often recycled after each build. Currently, a knowledge gap exists regarding powder reuse effects on powder size distribution, morphology, and chemistry as a function of part geometry and processing conditions. It was found during selective laser melting (SLM) of 316 stainless steel that a significant amount of (0.100 wt pct) oxygen pickup can occur in molten material (spatter) ejected from the powder bed surface. This value was significantly larger than the oxygen content of the as-received powder feedstock (0.033 wt pct). Furthermore, the powders in the heat-affected-zone regions, adjacent to molten pool, also exhibit oxygen pickup ($\geq 0.043$ wt pct). The oxygen content in unmelted 316L powder was found to vary as a function of its spatial position in the powder bed, relative to the heat source. Interestingly, the volume of melted material (*i.e.*, thin *vs* thick walls) did not correlate well with the extent of oxygen pickup. Possible mechanisms for oxygen pickup in the powder during SLM, such as adsorption and breakdown of water, oxygen solubility, spatter re-introduction, and solid-state oxide growth, are discussed.

## I. INTRODUCTION

METAL additive manufacturing allows for the manufacture of complex, near net-shape parts. Powder bed additive manufacturing processes require a metal powder feedstock, as well as a substrate on which to build, and employ either an electron beam or laser heat source to melt the powder in a succession of stacked and fused layers. This research focuses on identifying and describing local powder bed degradation during the selective laser melting (SLM) process.

It is well known in literature that laser parameter selection can influence the microstructure of SLM-processed material.[1–3] However, one of the economic advantages often attributed to powder bed additive manufacturing is that unmelted powder can be reused as feedstock for future builds. In reality, the recyclability of unmelted powders is not well understood for industrial usage due to the uncertainty over how powder degradation occurs and affects the properties of additively manufactured parts. As a result, the economic benefit from reusing powder is often avoided in industrial additive manufacturing processing facilities.

Powder recyclability studies have been performed in an attempt to understand and quantitatively verify the physiochemical changes in unmelted powder as a function of powder reuse. Tang *et al.* and Nandwana *et al.* have studied recycled Ti-6Al-4V powders during electron beam powder bed processing.[4,5] Tang's study incorporated 21 reuse cycles, with no change in part geometry or process conditions, and with periodic additions of fresh powder to the original reused powder bed. Nandwana's study restricted the blending of new powders with reused powder and achieved six reuse cycles. Both studies incorporated the following measurements to characterize the bulk properties of the recycled powder beds: Hall flow; powder size distribution (PSD); elemental chemical analysis; and surface roughness. These studies revealed an increase in oxygen content within the Ti-6Al-4V powder and parts as a function of reuse cycles. The authors attributed the oxygen increase to the high oxygen solubility of titanium and the repeated exposure of the powder to atmospheric

D. GALICKI is with the University of Tennessee Knoxville, 1512 Middle Drive, Knoxville, TN. Contact e-mail: dgalicki@gmail.com F. LIST is with the Oak Ridge National Laboratory, Oak Ridge, TN. S.S. BABU and A. PLOTKOWSKI are with the University of Tennessee Knoxville, 1512 Middle Drive, Knoxville, TN and also with the Oak Ridge National Laboratory, Oak Ridge, TN. H.M. MEYER III is with the Materials Science and Technology Division, Oak Ridge, TN. R. SEALS and C. HAYES are with the Y12-CNS Nuclear Complex, Oak Ridge, TN.

conditions during part unloading, powder recovery, and loading efforts. Interestingly, studies on powder recyclability during selective laser melting are limited. Liu *et al.* studied stainless steel 316L spatter in selective laser melting and its effect on the macroscopic properties of tensile specimens, prepared using a mixture of spatter and fresh powder.[6] They attributed the decreases in yield strength (YS) and ultimate tensile strength (UTS) to the lack of fusion defects and inclusions resulting from partially melted powders. Liu's work did not specify the mechanisms for such degradation, which could be attributable to either the processing conditions or powder characteristics. A recyclability study of Ti-6Al-4V powder, commissioned by Renishaw, also characterized the powder feedstock in terms of bulk, or average, properties.[7] Because of dilution effects, measurements of bulk powder characteristics may not be able to differentiate the localized changes in the powder bed close to the heat source and may not be representative of specific property changes induced by the AM process. This paper gives special attention to characterizing the powder directly adjacent to melt zones in the SLM process. These areas experience local thermal cycling and are most likely to experience property modifications resulting from exposure to the heat source. Contrary to electron beam melting, selective laser melting using today's commercial machines typically occurs in a nonvacuum environment, utilizing a constant flow of cover gas (*e.g.,* Argon) over the build surface. Unless efforts are made to purify the inert cover gas, possible gaseous reactants (*e.g.,* $O_2$, $N_2$, $C_xH_y$, $H_2O$) may adsorb on the powder feedstock and result in oxide formation during the SLM process. Because metal additive manufacturing resembles traditional welding in many aspects, prior knowledge regarding solid-state oxidation and oxide formation during welding can help to guide additive manufacturing research.

### A. Solid-State Oxidation

Ellingham diagrams reveal that $Cr_2O_3$ oxides are the most thermodynamically stable of the metal oxides and are therefore predicted to form first before all other oxides. $Cr_2O_3$ forms at an oxygen partial pressure of just $10^{-13}$ mbar at the melting temperature of 316L steel (1400 °C). It is followed in stability in the following order by FeO ($10^{-9}$ mbar), $Fe_3O_4$ ($10^{-4}$ mbar), NiO ($10^{-3}$ mbar), and $Fe_2O_3$ ($10^2$ mbar).[8] Alloying elements within stainless steel 316L can also form oxides at this temperature: MnO at $10^{-15}$ mbar, and $SiO_2$ at $10^{-17}$ mbar $O_2$ partial pressures. SLM machines operate at oxygen partial pressures of $10^{-3}$ to $10^{-2}$ mbar (see Section III–A), indicating that some amount of oxide formation both within the weld pool and in the powder feedstock itself is likely during the SLM process, with the oxide amount dependent on the kinetics of oxide formation and growth. Reviews of low- and high-temperature oxidation of metals can be found in References 9 and 10.

Traditional oxidation studies of steel measure the weight gain or loss of the steel over time while exposed to oxidizing temperatures and environments over a time span of hours. These continuous studies allow for the study and definition of the complete kinetic record of the oxidizing reaction at a specific temperature.

Stainless steel oxidation literature reveals that a range of oxides may form ($Cr_2O_3$, FeO, $Fe_2O_3$, $Fe_3O_4$, NiO, and spinel).[11,12] Kinetics of these oxide growths is complicated by the various diffusion rates of metal and oxygen ions through the different oxide phases, and the varying degrees of solubility of the oxides in one another.[13] Tarabay *et al.* investigated the oxidation of a 304L stainless steel, water-atomized powder *via* thermogravimetric analysis held at 800 °C under a helium–oxygen mixture for 6 to 20 hours, and found that it oxidized akin to convential stainless steel plate, exhibiting parabolic-like behavior.[14]

The amount of time that unmelted steel powder is exposed to high temperatures during the SLM process is typically on the order of seconds as opposed to the minutes or hours, making the measurement of these oxides by traditional methods difficult and the development of a predictive model preferable. This work attempts to develop such a model using simple well-known formulas like the Rosenthal heat equation in conjunction with widely available thermodynamics and kinetics software like ThermoCalc and DICTRA.

### B. Oxidation Phenomenon During Welding

Hibiya and Debroy have calculated the change in surface tension gradient of molten iron as a function of oxygen partial pressure above as well as the oxygen addition to the melt pool.[15,16] As oxygen is added to the weld pool, the surface tension gradient of molten iron experiences a negative-to-positive shift in sign value. This sign shift in surface tension gradient can affect the convective flow pattern within the melt pool and can consequently affect the melt pool aspect ratio. In selective laser melting, the consequences of a changing weld pool width and depth could be realized as decreased overlap between melt tracks and/or decreased bonding between melt layers. Both of these consequences have the potential to increase lack of fusion porosity in the final part. Louvis *et al.* have shown that preexisting aluminum oxides can affect the solidification of the weld pool during SLM processing of aluminum alloys.[17] Thin oxide layers that form at the initial liquid–solid interface during SLM solidification can interfere with epitaxial solidification of the weld pool, reducing the bond strength between melt layers. In SLM, it is conceivable that oxide seeds could be introduced into the melt pool *via* the breakup of surface oxides on the metal powder feedstock. Since it is preferable to reduce inclusions, a strong motivation exists to limit the extent of oxide formation both on the powder prior to SLM processing and the powder/part system during SLM processing. This forms the motivation for the current research. Our specific focus is related to the observing and explaining the oxide formation in the heat-affected-zone (HAZ) regions of the powder bed near to the part perimeter.

## II. EXPERIMENTAL PROCEDURE

### A. SLM Processing Plan

A Renishaw AM250 instrument with a maximum laser power of 200W was used to conduct three heat-affected-zone experiments (HAZ1, HAZ2, and HAZ3). The Renishaw AM250 build process uses a pulsed laser to selectively melt regions of a metal powder bed. Melting bonds the powder layer to either the tool steel build plate or previously melted layers. Virgin stainless steel 316L powder purchased from Renishaw was used as the feedstock in all of the HAZ experiments. Before starting the process, the build chamber was evacuated and refilled with a nonreactive argon cover gas. A purge and refill cycle was conducted until the chamber oxygen content measured below 0.02 mbar. During the SLM process, the argon cover gas was constantly recirculated over the powder bed surface and through a filter using a fan set at a recirculating speed of 22 Hertz. The volumetric flow rate of the chamber gas as well as the type of flow over the powder bed (laminar $vs$ turbulent) is unknown. Other relevant process parameters are given in Table I, and a full list of machine parameters can be found in Appendix A. Parameter selection and slicing of the CAD part was conducted using AutoFab v1.8.

The heat-affected-zone experiments were designed to provide information from the unmelted powder bed regions, measured as closely as possible to a melted region during selective laser melting. All three of the HAZ experiments were designed to have walls of processed material spaced at regular intervals to each other. This spacing created channels where unmelted powders were retained. The number of channels for a given spacing was chosen to keep the total volume of powder (~ 1 cm$^3$) contained within the channels approximately constant across each channel spacing value. As the spacing between the channel walls decreased, the fraction of unmelted powder within the channel that was exposed to the heat given off by the melting of the channel walls increased. Powder samples collected from the channels post process were analyzed for phase change, oxygen content, and powder size distribution changes. The designs of the three experiments were necessarily focused on gradual changes. It was found during powder collection that the 100-$\mu$m-wide channel walls in the HAZ1 experiment (Figure 1) were too thin and would break and mix with the powder during collection of the 150-$\mu$m channel powder, contaminating the sample.

### Table I. Renishaw AM250 Processing Parameters During HAZ Experiments

| | | |
|---|---|---|
| Power | 200 | W |
| Focus Offset | 0 | mm |
| Point Distance | 60 | $\mu$m |
| Exposure Time | 80 | $\mu$s |
| Angle Increment | 67 | deg |
| Hatch Spacing | 110 | $\mu$m |

The HAZ1 experiment was redesigned and repeated in the HAZ2 experiment as shown in Figure 2. The HAZ2 design featured channel walls of 150 $\mu$m thickness that did not break during sample collection. The HAZ2 design also physically spaced channel sections from each other in order to eliminate any contributing heat effects between channel sections.

The HAZ3 experiment was designed to investigate the effect of channel wall thickness on the heat-affected zone within the channels. This experiment chose two extremes in both the channel wall thicknesses (150, 2000 $\mu$m) and channel widths (150, 5000 $\mu$m) and combined them into the four distinct sections shown in Figure 3.

Powder samples were collected from each channel width section of all three experiments by covering all of the noncollection channels with an aluminum plate that had a rubber pad glued onto one face, and then turning the entire baseplate upside down to allow powder to flow out of the open channel and onto an aluminum foil sheet. C-clamps were used to ensure that the rubber pad made a strong seal against the channel wall surfaces, thereby preventing the mixing of powders between channels during powder removal. Powder samples were



Fig. 1—Top-down view of heat-affected-zone experiment #1: 5-, 4-, 3-, 2-, 1-mm-wide, 500-, 350-, 250-, and 150-$\mu$m-wide channels separated internally by 100-$\mu$m-thick walls.



Fig. 2—Top-down view of heat-affected-zone experiment #2: 5, 4, 3, 2, 1 mm, 500-, 350-, 250-, and 150-$\mu$m-wide channels separated internally by 150-$\mu$m-thick walls.
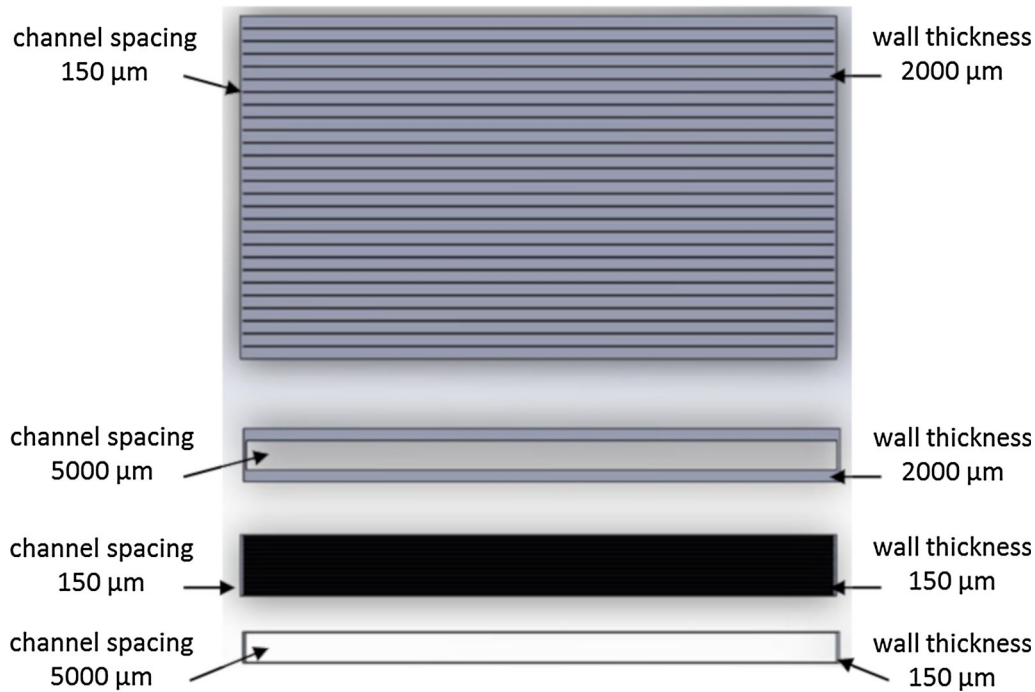
Fig. 3—Heat-affected-zone experiment #3: 5 mm-wide channel with 150-$\mu m$-thick walls, 5 mm channel with 2-mm-thick walls, 150-$\mu m$ channels with 150-$\mu m$-thick walls, and 150-$\mu m$ channels with 2-mm-thick walls.

stored in separate glass vials designated by their experiment number (HAZ1, HAZ2, or HAZ3) and channel widths/wall thicknesses.

## B. *Data Collection and Characterization*

Build chamber gas partial pressure was monitored, and X-ray diffraction for phase analysis, laser diffraction for size distribution, bulk chemical analysis for oxygen content, and X-ray photoelectron spectroscopy for surface composition were performed on the heat-affected-zone powder samples in an attempt to identify a heat-affected zone within the unmelted powder directly adjacent to melt zones.

### 1. *Oxygen partial pressure*

Renishaw AM250 log files records of the chamber gas pressure (mbar) and oxygen content (ppm) during each of the heat-affected zone experiments. The system utilizes two recirculation oxygen sensors to monitor build chamber oxygen content. One sensor is located in line with the gas recirculation system at a point just before the gas enters the filter, or the "bottom" position. The second sensor is located at a point in the recirculation system just before the vent, or the "top" position. Proprietary Renishaw software used the values from these sensors to report oxygen content in units of parts per million (ppm). The oxygen partial pressure ($p_{O_2}$) was calculated from the measured chamber pressure and oxygen ppm values. The oxygen data presented in this paper were collected from the "bottom" sensor, as it measures the gas coming directly from the build chamber and before filtration, and is therefore considered a truer indicator of the actual $O_2$ value within the build chamber cover gas than the sensor located in the "top" position.

### 2. *X-ray diffraction*

X-ray diffraction was performed on the 150-, 500-, and 5000-$\mu m$ channel width powder samples from the first two heat-affected-zone experiments as well as all four of the channel width/wall thickness combinations in the third heat-affected-zone experiment. Samples were analyzed using a Bruker D2Phaser desktop diffractometer.[8] This instrument utilizes a Cu X-ray source which is filtered with Ni foil to limit beam output to only the Cu K$\alpha_1$ (1.540562 Å) and K$\alpha_2$ (1.54439 Å) wavelengths. The detector used was a LYNEYE™ 1-dimensional area detector based on Bruker AXS' compound silicon strip technology.[19] Data from the powder were collected using a beam voltage and amperage of 30 kV and 10 mA, respectively. A detector dwell time of 0.5 seconds was used. In addition, Virgin powder X-ray diffraction was conducted using the ORNL Material Science and Technology Division (MST) Panalytical X'pert diffractometer. Scans were performed from nominally 5 to 45 deg $2\theta$ in 1-hour scans using a generator voltage of 55 kV, a tube current of 40 mA, Mo K$\alpha$ radiation ($\lambda_{k\alpha 1} = 0.709319$ Å, $\lambda_{k\alpha 2} = 0.713609$ Å), and the X'Celerator detector. ¼ deg fixed slits, ½ deg anti-scatter slit, and 0.02 soller slits coupled with a 10-mm mask (beam length) were used during the measurements. The powder samples were loaded into deep wells, and a spinner stage (4 seconds/rev) with an automated sample changer was used. To more easily compare the results from the two different machines, the 2-theta range of the Mo source was converted to a Cu 2-theta range using the conversion.

$$\theta_{\text{Cu}} = \arcsin\left[\frac{\lambda_{\text{Cu}}^{\text{avg}}\sin(\theta_{\text{Mo}})}{\lambda_{\text{Mo}}^{\text{avg}}}\right], \qquad [1]$$

where $\theta_{\text{Cu}}$ is the converted detection angle for a copper X-ray source, $\lambda_{\text{Cu}}^{\text{avg}}$ is an average of the two Kα X-ray wavelengths emitted by a copper source, $\theta_{\text{Mo}}$ is the measured detection angle from molybdenum x-ray source XRD measurements, and $\lambda_{Mo}^{avg}$ is the average of the two Kα x-ray wavelengths emitted by a molybdenum source.

### 3. *Powder size distribution*

Horiba La950 V2 Laser Diffraction Particle Analyzer was used to analyze the size distribution of powder collected from the 150-, 250-, 350-, 500-, and 1000-$\mu$m channels from the HAZ2 experiment, and all four sections from the HAZ3 experiment. Powder samples from the HAZ1 experiment were not measured for size distribution due to their expected similarity to powder collected from the HAZ2 experiment. Furthermore, as mentioned earlier, broken pieces of channel wall had contaminated the 150-$\mu$m channel powder sample from HAZ1.

### 4. *Chemical analysis*

Samples taken from powder originating in the 150-, 500-, and 5000-$\mu$m channels from the HAZ1 and HAZ2 experiments, as well as all four of the channel width/wall thickness combinations in the HAZ3 experiment, were sent to Luvak Laboratories for chemical analysis of the bulk oxygen content within the powder. Luvak determined the oxygen content in the samples by following instructions laid out in ASTM E 1019-11.[20] Oxygen analysis results from the HAZ1 150-$\mu$m channel width powder sample (see Section III–B) may be considered suspect if the oxygen content of the broken wall contaminants differ from that of the adjacent powder.

A virgin powder sample was also heated in an oven for 1 hour at 110 °C and subsequently tested for oxygen content. The oxygen content of the heated virgin powder sample was compared to the oxygen content of an unheated virgin powder sample.

### 5. *X-ray photoelectron spectroscopy (XPS)*

Virgin powder and samples taken from the powder originating in the 150-$\mu$m channels from the HAZ1 and HAZ2 experiments were examined using XPS at ORNL's MST Division. Powder samples were placed on a double-sided strip of carbon tape. A monochromatic Al k-alpha X-ray source, angled 54 deg relative to the X-ray detector was used. The photo-electron detector was positioned normal to the surface sample. An argon-ion gun, positioned 45 deg relative to the detector, was operated at 2 kV and had a calibrated sputtering rate of 12 nm/min. The sputtering rate was calibrated using $SiO_2$ films. Measurements were taken over an elliptical area measuring 375 $\mu$m along the semi-major axis and 175 $\mu$m along the semi-minor axis for 510 (virgin), 585 (HAZ2), and 735 (HAZ3) seconds, respectively. Assuming 2D circle packing and a mean particle size of 30 microns, the measured area

encompassed anywhere from ~ 145 (50 pct packing density) to ~ 260 (90 pct packing density) powder particles. Samples were not rotated during data collection.

## III. RESULTS

### A. *Variations of Oxygen Partial Pressure during SLM*

The partial pressure of oxygen inside the build chamber of the Renishaw AM250 varied as a function of time. At the start of a build, $O_2$ values of around 800 ppm and a chamber gas pressure of 20 mbar were typical. The corresponding oxygen partial pressure at this chamber pressure and oxygen ppm content were calculated to be 0.016 mbar. Due to a small leak in the system, the chamber gas pressure began at 20 mbar and slowly decreased to 6 mbar over the course of a couple of hours. Once 6 mbar was reached, the Renishaw would introduce fresh argon into the build chamber, and the chamber pressure would correspondingly jump back to 20 mbar before slowly decreasing back to 6 mbar. Because of the periodic variance in the chamber gas pressure, the $O_2$ partial pressure also cycled between 0.016 and 0.0048 mbar until about 6 hours into a build. At about 6 hours, the machine's oxygen sensors generally read 0 ppm oxygen and an oxygen partial pressure could not be calculated.

The calculated $O_2$ partial pressures throughout the entire build for each HAZ experiment are given in Figure 4. The average $O_2$ partial pressure experienced by the powder during each experiment also given in Figure 4 is seen to generally agree between builds. It can be seen that $O_2$ partial pressures can vary between builds but generally stays below 0.015 mbar due to the manually set limit of 0.02 mbar. If the Renishaw AM250 detects an $O_2$ value greater than 0.02 mbar, then $O_2$ automatically pauses the SLM process and enters into vent and backfill mode until the recorded ppm value of $O_2$ falls below 0.02 mbar. This vent-and-backfill cycle is evident in Figure 4 at the beginning of each of the HAZ experiments. HAZ1 and HAZ2 $O_2$ partial pressures both follow a typical
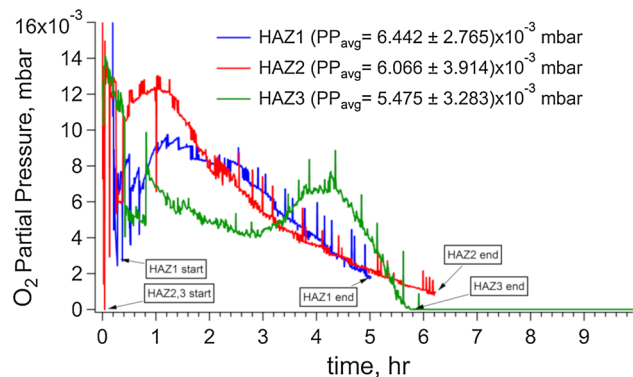


Fig. 4—Bottom oxygen sensor values and the corresponding calculated oxygen partial pressures in an otherwise pure argon environment during processing of the three heat-affected-zone experiments.

decrease of measured $O_2$ over time assumed to be brought on by gettering of oxygen by the SLM material, reactions of oxygen with evaporated metal species, and the periodic introduction of argon into the chamber to bring the chamber pressure back to 20 mbar once it falls below 6 mbar. The HAZ3 $O_2$ partial pressure exhibits an atypical rise in oxygen partial pressure at around the 3-hour mark before resuming its decrease at around the 4.3-hour mark. It is hypothesized that the initial increase in oxygen partial pressure in all three of the HAZ experiments is due to oxygen introduced from the powder hopper as it dispenses fresh powder for each new layer. Over time, all of the oxygen that was trapped in the powder within the hopper is released, and $O_2$ partial pressures are allowed to decrease again. This explanation could also explain the atypical $O_2$ partial pressure curve observed for the HAZ3 experiment. In this case, trapped oxygen from powder within the hopper could have been released partly into the build rather than entirely at the beginning.

### B. *Chemical Analysis*

#### 1. *HAZ1 and HAZ2 chemistry*
Excepting the 150-$\mu$m data point from the first HAZ experiment (due to possible contamination by broken wall pieces) the oxygen content measurements from the HAZ1 and HAZ2 samples provide evidence for reproducibility within the error of measurement. Figure 5 shows that the powder oxygen content (wt pct) decreases as a function of channel width, with a measurable increase in powder residing in the 500-$\mu$m-wide channel and no measurable increase in powder residing in the 5000-$\mu$m-wide channel. The data from these three channel spacings was deemed sufficient and the powders from the other channel width spacings were not chemically tested for oxygen content.

#### 2. *HAZ3 chemistry*
The HAZ3 experiment varied the channel wall thickness between 150 and 2000$\mu$m and the channel widths
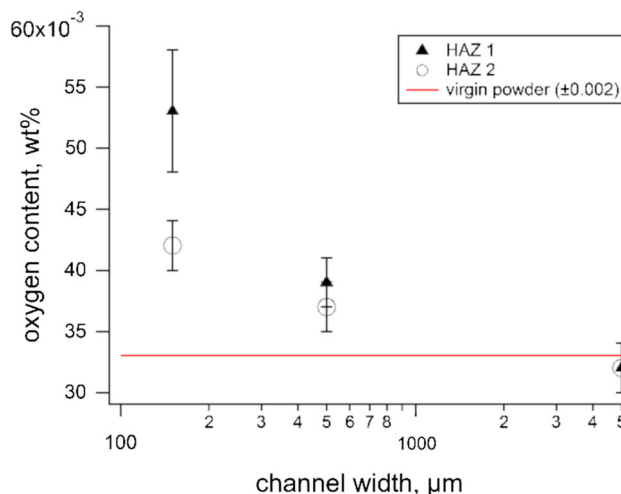


Fig. 5—Unmelted powder oxygen content (wt pct) as a function of channel width between melted walls.

between 150- and 5000-$\mu$m. Figure 6 shows that the thickness of the channel walls in the HAZ3 experiment did not affect the measured oxygen content of the unmelted powder within the channels themselves.

### C. *X-Ray Diffraction*

Figure 7 shows the XRD results of powder samples from the virgin powder and all three heat-affected-zone experiments. All of powder samples revealed fully austenitic phase and no detectable evidence for any other phases. The bimodal peaks present in these plots correspond to the slightly different wavelengths of the X-ray radiation given off by the Cu and Mo diffractometer X-ray sources. Both Molybdenum and Copper sources each emit two characteristic $k_{\alpha}$ X-rays at differing wavelengths. The data obtained from the Mo X-ray sources were converted to Cu source values using Eq. [1] to facilitate comparison between the virgin powder and the HAZ experiments powder samples.

### D. *Powder Size Distribution*

Figures 8, 9 and Tables II and III show the powder size distribution data obtained from laser diffraction measurements from the selected channels of the HAZ2 and HAZ3 experiments. A slight coarsening seems to be present in HAZ2 samples from channel widths of 150, 250, and 1000 $\mu$m, and a widening of the powder size distribution occurs in samples from channel widths of 250, 500, and 1000 $\mu$m. The powder size distribution average is slightly smaller in the HAZ3 samples when compared to virgin powder. It is worth noting that all powder sample size distributions were only measured once, with an assumption that the uncertainty related to sampling procedures are minimal.

### E. *X-Ray Photoelectron Spectroscopy (XPS)*

Even though the depths associated with the XPS measurements shown in Figure 10 are calibrated using $SiO_2$ films instead of stainless steel, the qualitative results can be analyzed to understand aspects of the powder samples' surface chemistry. In Figures 10(a) through (d), virgin powder contains a higher percentage of iron associated with iron oxides than do the HAZ2 and HAZ3 powder samples. Conversely, the HAZ2 and HAZ3 powder samples contain a higher percentage of chromium associated with chromium oxides than does the virgin powder sample (Figures 10(a) through (c), (e)).

Interesting peaks in Figures 10(a) through (e) are present at distances several nanometers below the surface of the powder particles. These peaks are likely an effect of the sample surface morphology, namely that the samples are not flat but are instead composed of many spheres packed closely together. When the argon-ion beam first begins to sputter away material, what is measured is the surface data of the particles. Because of the powder particles' rounded surfaces and the 45 deg angle at which the ion gun is situated relative to the sample, individual powder particles can "shade"
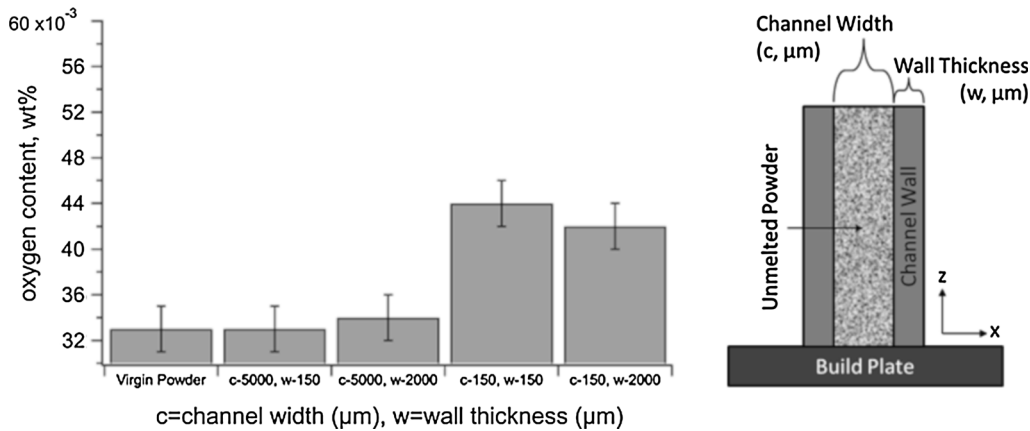
Fig. 6—Bulk chemical analysis of powder samples taken from several sections of the third heat-affected-zone experiment. Error values of ± 0.002 wt pct were provided by Luvak Laboratories.
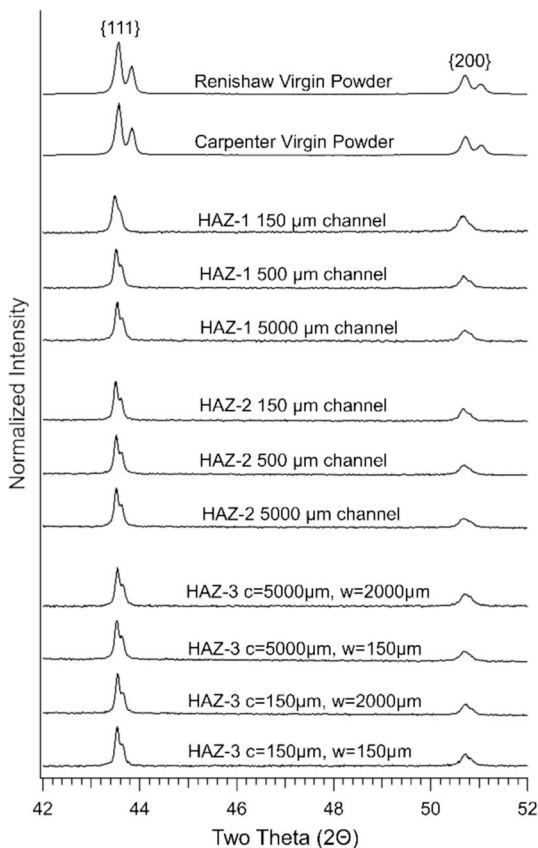


Fig. 7—X-ray diffraction peaks of virgin powder and powder samples collected from the HAZ1, HAZ2, and HAZ3 experiments. FCC crystal structures were seen with no evidence of additional phases. A Mo X-ray source was used to collect the virgin powder data, and a Cu X-ray source was used to collect the HAZ experiments' data. c: channel width, w: wall thickness.

adjacent particles temporarily. Once enough material is sputtered away, the shaded adjacent particles are then exposed to the ion beam, and the fresh surface area is measured. This effect continues until no more particles are shaded by their neighbors.

Figure 10(f) confirms the presence of chromium in increased amounts relative to iron at the HAZ powder surfaces. The total chromium-to-iron ratio (Cr/Fe) was calculated at each measurement point. This value was compared as a ratio to the Cr/Fe ratio of the bulk material (Cr/Fe-bulk). The Cr/Fe-bulk value was taken to be the mean of the last ten data points. Figure 10(f) shows that chromium enrichment at the surface of the HAZ particles is increased relative to virgin powder. The enrichment is pronounced at the surface and can be seen at deeper surface levels in the HAZ powder compared to the virgin powder. If the maximum oxide depth is taken to be the point when the slope levels off in Figure 10(f), then the oxide depths for the virgin, HAZ2, and HAZ3 powders are approximately 10, 15, and 24 nm, respectively.

## IV. DISCUSSION

XRD and PSD measurements of the heat-affected-zone powders reveal that neither the powder size nor the crystallographic structure of unmelted powder is affected by their proximity to melt regions during the SLM process. The observed oxygen wt pct increase in the HAZ samples (see Figures 6 and 7) cannot be explained by the dissolution in the molten state or by the loss of materials that are devoid of oxygen. At normal processing atmospheric pressures, evaporation loss of non-oxygen containing material may only occur at temperatures above the boiling point of the material or due to dissociation of oxides, e.g., 1100 °C for oxide to gas reactions.[9] Boiling temperatures were obviously not reached in the heat-affected zones of interest and only a small fraction of the HAZ powder reaches high enough temperatures for oxide to gas reactions, according to a Rosenthal heat conduction model. The oxygen increases in the heat-affected zones can be concluded to be the result of a physical mechanism, yet to be understood. Three of the most likely methods of oxygen addition, i.e., rapid oxide formation, spatter, and moisture retention are discussed in this section.
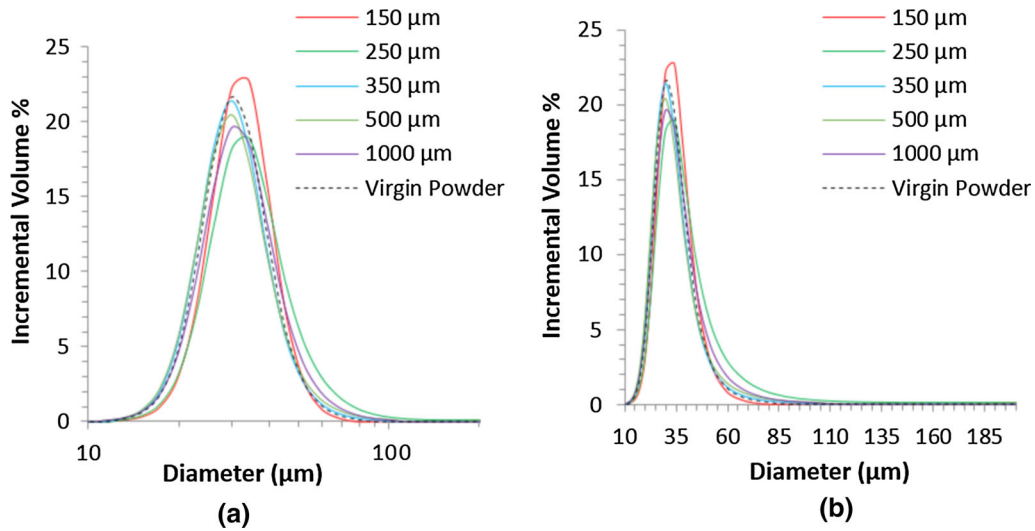
Fig. 8—Laser diffraction results for samples collected from the HAZ2 experiment, compared to virgin powder. Presented here in log (*a*) and linear (*b*) forms.
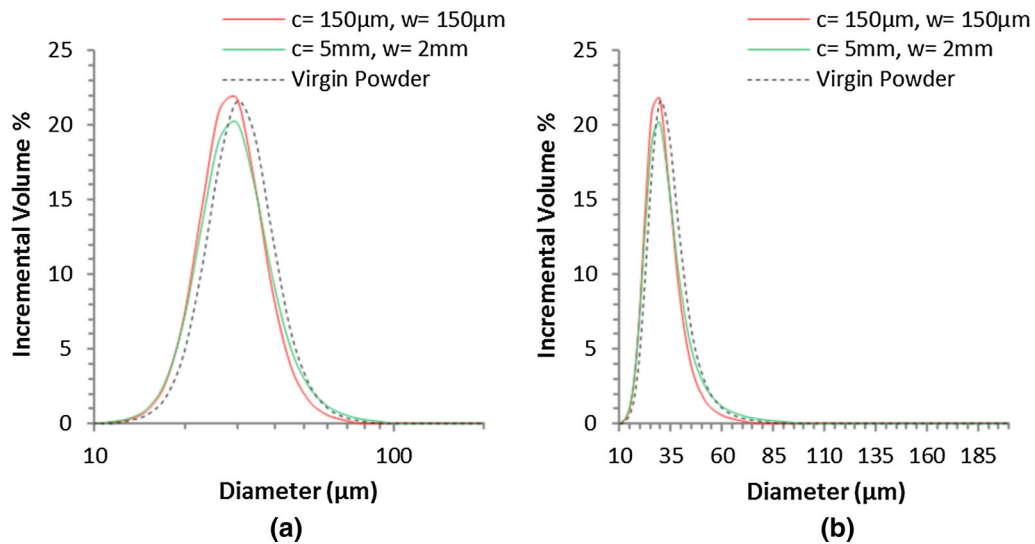


Fig. 9—Laser diffraction results for samples collected from the HAZ3 experiment, compared to virgin powder. Presented here in log (*a*) and linear (*b*) forms. c: channel width, w: wall thickness.

## A. *Role of Moisture*

Water vapor has the potential to accelerate the observed oxidation kinetics in steels and other metals noticeably.[9] However, most of these effects apply to fully developed scales and are only observable after temperature exposure times far exceeding that seen by unmelted powder during SLM. It is worth noting that any pick up of moisture from the environment by the feedstock powder may contribute to the introduction of oxygen into the system. The 316L powder was stored in a climate-controlled high bay area for several weeks in closed containers containing desiccant bags. However, once the powder containers were opened, the desiccant bags were removed, and the powder left exposed to air for sometimes several hours. No drying of the powders was employed, so whatever moisture that was picked up

as powder was transferred to the sieve and back to the Renishaw AM 250 hopper is likely retained prior to its use as feedstock. The oxygen chemical analysis results do not support this theory of oxygen addition to the powder bed. Figure 5 shows that the oxygen values for the powder samples taken from the 5000-*μm* channel spacings in both HAZ1 and HAZ2 experiments equal the oxygen values of the fresh powder before it is processed (Figure 6).

Powder samples were also dried in an oven at 110 °C for one hour prior to oxygen analysis, and the results were compared to oxygen analysis of powders in the undried state. No difference in oxygen content could be detected between the dried and undried powder samples, further discrediting the theory of retained moisture adding measurable amounts of oxygen into the system.

**Table II. Median, Mean, Mode, $D$(v,0.1), $D$(v,0.5), and $D$(v,0.9) Values for the Powder Size Distribution Samples from the HAZ2 Experiment**

| HAZ_2 Channel Width ($\mu$m) | Median ($\mu$m) | Mean ($\mu$m) | Mode ($\mu$m) | St. Dev. ($\mu$m) | D(v, 0.1) ($\mu$m) | D(v, 0.5) ($\mu$m) | D(v, 0.9) ($\mu$m) |
|---|---|---|---|---|---|---|---|
| 150 | 29.99 | 30.76 | 31.41 | 7.44 | 21.95 | 29.99 | 40.52 |
| 250 | 31.32 | 34.66 | 31.63 | 17.76 | 21.85 | 31.32 | 48.47 |
| 350 | 28.13 | 29.46 | 27.93 | 8.59 | 20.25 | 28.13 | 39.95 |
| 500 | 28.12 | 30.53 | 27.88 | 15.55 | 20.05 | 28.12 | 41.53 |
| 1000 | 29.38 | 31.07 | 28.22 | 10.00 | 20.55 | 29.38 | 43.35 |

**Table III. Median, Mean, Mode, $D$(v,0.1), $D$(v,0.5), and $D$(v,0.9) Values for the Powder Size Distribution Samples from the Third Heat-Affected Zone Experiment**

| HAZ_3 Channel Width (c), Wall Thickness (w) ($\mu$m) | Median ($\mu$m) | Mean ($\mu$m) | Mode ($\mu$m) | St. Dev. ($\mu$m) | D(v, 0.1) ($\mu$m) | D(v, 0.5) ($\mu$m) | D(v, 0.9) ($\mu$m) |
|---|---|---|---|---|---|---|---|
| $c = 150$, $w = 150$ | 26.68 | 27.66 | 27.53 | 7.33 | 19.41 | 26.68 | 37.25 |
| $c = 5000$, $w = 2000$ | 27.24 | 28.75 | 27.66 | 9.00 | 19.32 | 27.24 | 39.54 |

## B. Rapid Oxidation of Powders

Solid-state growth of a surface oxide shell surrounding a powder particle is the most likely mechanism to explain the oxygen pickup observed in the powder bed HAZ. Oxygen has a low solubility in FCC iron (0.0002 wt pct) and cannot therefore exist as solute within the powder particle lattice structure. Surface moisture retention was ruled out by a heating experiment (Section IV–A). The following sections attempt to estimate the amount of oxide shell growth by first, back calculating from the measured bulk oxygen wt pct values given in Section III–B, and second, comparing the back-calculated oxide growth values to that determined by thermal heat-transfer model in combination with the DICTRA software. The heat-transfer model is based on the Rosenthal equation and was used to estimate the accumulated time period over which the HAZ powders were exposed to oxide-accelerating temperatures (>500 °C). The thermal histories output by the heat-transfer model were used as inputs into a DICTRA oxide growth model to model the amount of growth experienced by the oxide shell.

### 1. Solid-state oxidation back calculation

The back-calculated oxide thicknesses in this section were calculated using the measured oxygen content of powder particles both before and after thermal cycling (0.033 ± 0.002 and 0.043 ± 0.002 wt pct, respectively). They were performed to estimate the extent of oxide growth experienced by powder particles during processing. The details of the back calculation method are given in Appendix B.

The difference between the initial back-calculated average initial oxide thickness and the thermally cycled average oxide thickness is taken to be the oxide growth experienced by a single representative powder particle residing in the heat-affected zone. Real stainless steel oxides can be complex. To simplify the back calculation,

the assumption was made that the entire oxide shell surrounding a powder particle is made up of a single oxide type (i.e., FeO, $Fe_2O_3$, $Fe_3O_4$, $Cr_2O_3$). As a conservative estimate, it is also assumed that all oxygen pickup by the powder bed is converted to oxide scale, and that none of the initial oxygen or oxygen pickup is in the form of internal oxides, solutionized oxygen, or adsorbed $H_2O$. The back-calculated initial oxide thicknesses and heat-affected zone oxide growth values are presented in Table IV and take into account the oxygen content measurement error of 0.002 wt pct.

Figure 11 shows the calculated oxide scale growth needed to match the observed oxygen data (0.043 ± 0.002 wt pct). Each particle in the powder bed would need to grow, on average, a FeO oxide scale of 3.49 (± 1.05) nanometers, a $Fe_2O_3$ oxide scale of 2.83 (± 0.85) nanometers, a $Fe_3O_4$ oxide scale of 3.12 (± 0.94) nanometers, or a $Cr_2O_3$ oxide scale of 3.84 (± 1.16) nanometers, in addition to whatever passivation layer existed before the laser welding heat cycle(s). These values will be compared to the DICTRA-calculated oxide growth behavior in the following sections.

### 2. Dilution effects

The heat-affected-zone experiments bring to light a previously unknown phenomena in laser powder bed additive manufacturing: local changes (i.e., oxidation) can occur within the powder bed, and that these changes can escape bulk characterization detection by virtue of dilution. The diluting effects of non-oxidized powder mixed with and measured alongside oxidized powder are demonstrated in Figure 12. The measured oxygen values from the HAZ2 experiment lie within the range predicted by dilution by non-oxidized powder and demonstrate how easily localized powder characteristics can be obscured during bulk powder characterization. The upper and lower limits of oxidation were calculated by considering the 0.002 wt pct error of the processed
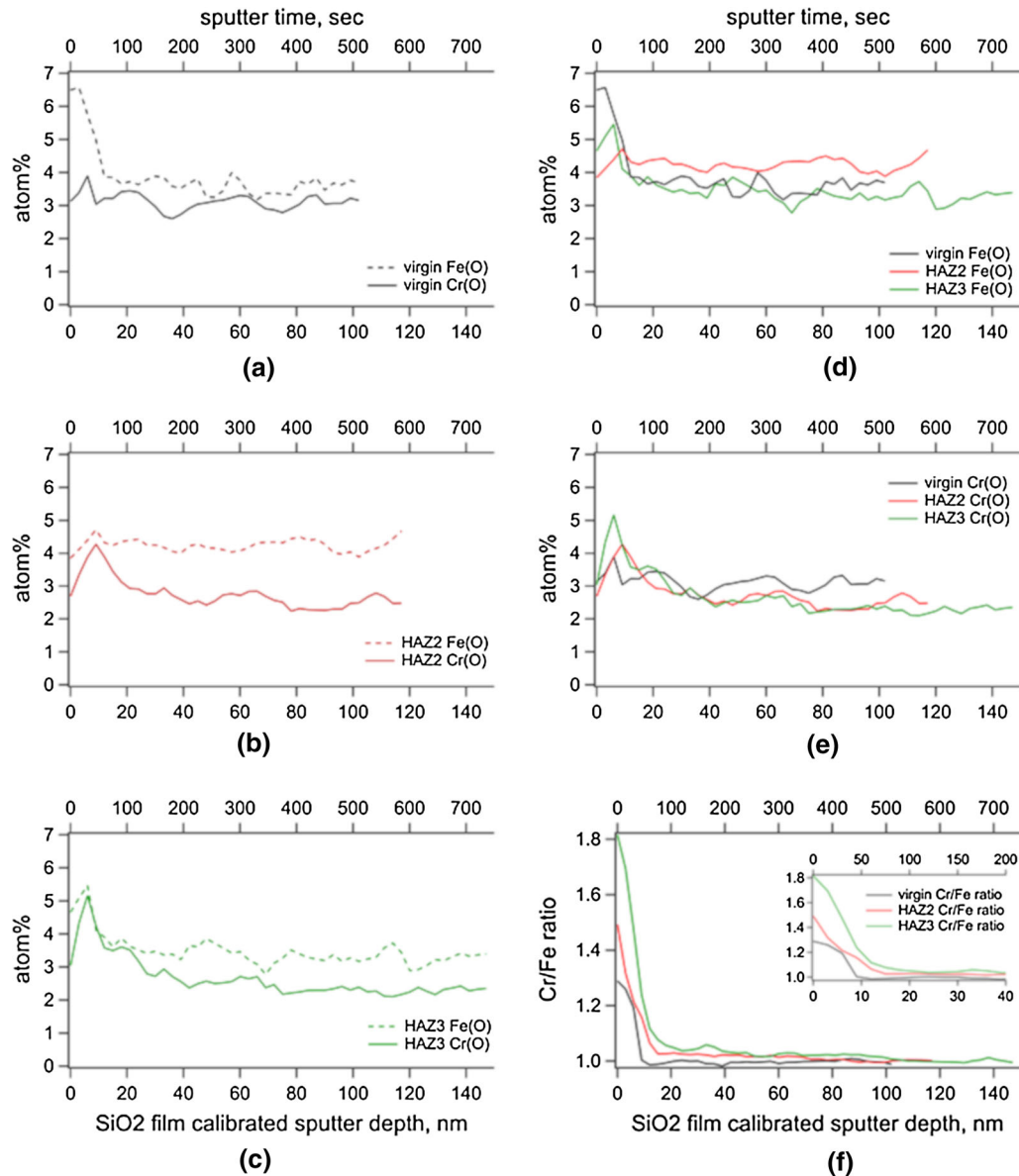
Fig. 10—XPS measurements of iron and chromium atoms associated with oxides on the surface of (*a*) virgin powder, (*b*) HAZ2 powder, and (c) HAZ3 powder. (*d*) Comparison of surface iron-oxide contents. (*e*) Comparison of surface chromium-oxide contents. (*f*) Comparison of (Cr/Fe)/(Cr/Fe-bulk) ratios.

powder oxygen content and assuming that all oxidation effects occur within 75 microns from the melted region (150-micron channel width). Details of the method used to calculate the dilution effect can be found in Appendix C.

### 3. *Thermal cycle and oxidation modeling*

DICTRA was used to model the oxidation of an FCC iron substrate with an initial spinel ($Fe_3O_4$) oxide layer. Previous literature suggests that initial oxide layers in metal powder used for additive manufacturing are on the order of 3 nm,[21] but 9.036 nm was used here in order to be consistent with the conservative, maximum value found by back calculation in Section IV–B–1, and does not appreciably change the DICTRA model results

when compared to a 3 nm starting value. The thermal histories of the unmelted powder were obtained from a heat-transfer model and input into DICTRA to calculate oxide shell growth.

While more advanced methods exist to model the thermal profile of the powder bed,[22] the Rosenthal heat equation is used here in an attempt to reduce the complexity of the model as much as possible. The Rosenthal heat equation was used to model the steady state temperature field in the surrounding powder during laser processing, ignoring thermal effects of the thin wall substrate directly below the laser. Rosenthal presented an equation describing the steady-state temperature distribution for the case of a steady-state, point heat source[23]:

**Table IV. Back-Calculated Initial Oxide Thicknesses, Heat-Affected Zone Oxide Thickness, and the Resulting Oxide Growth Values for FeO, Fe₂O₃, Fe₃O₄, and Cr₂O₃ Oxide Shells**

| | Volume Averaged Particle Diameter, $D_V$ = 27.71 microns | | |
|---|---|---|---|
| Oxide | Initial Thickness (nm) | HAZ Oxide Thickness (nm) | Oxide Growth, (nm) |
| FeO | 8.95–10.10 | 11.83–13.91 | 1.73–4.97 |
| Fe2O3 | 7.26–8.20 | 9.61–11.30 | 1.41–4.03 |
| Fe3O4 | 8.00–9.04 | 10.59–12.45 | 1.55–4.44 |
| Cr2O3 | 9.84–11.11 | 13.01–15.30 | 1.90–5.46 |
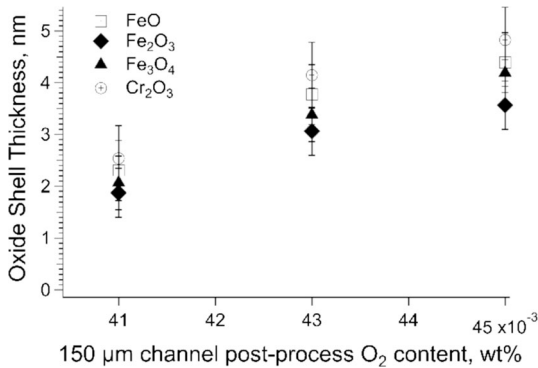


Fig. 11—Back-calculated oxide shell thickness increase assuming FeO, Fe₂O₃, Fe₃O₄, or Cr₂O₃ oxide growth.
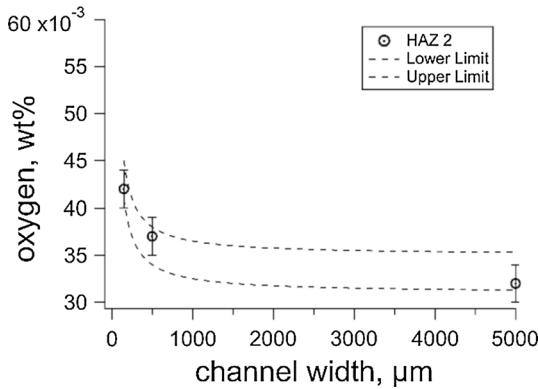


Fig. 12—HAZ2 measured bulk oxygen content with maximum and minimum calculated dilution effects indicated by dashed lines.

$$T(x, R) = T_0 + \frac{\eta VI}{2\pi\lambda}\left(\frac{1}{R}\right)\exp\left\{-\frac{v}{2a}(R+x))\right\}, R = \sqrt{x^2 + y^2 + z^2} \quad [2]$$

where $T(x, R)$ is the temperature as a function of radial distance $(R)$ and linear distance $(x)$ along the weld centerline, $T_0$ is the preheat or interpass temperature, $V$ the arc voltage, $I$ the welding current, $v$ the welding speed, $a$ the thermal diffusivity, $\eta$ the arc efficiency, and $\lambda$ the thermal conductivity. The thermophysical properties used in the conduction model are listed in Table V. In laser welding, the $\eta VI$ term can be replaced with an effective absorbed power ($P_{abs} = P \cdot \lambda_{abs}$). When only

surface temperature distributions are of interest, one only has to omit the $z$ variable in Eq. [2].

Because a pulsed laser system was used to conduct the HAZ experiments, an effective weld speed $v_{eff}$ was used as the velocity input into Eq. [2]. $v_{eff}$ was calculated by adding together the total distance traveled by the laser after a large number of pulses and then dividing by the total laser travel time according to equations

$$t_{tot} = n(t_{exp} + t_{set}) + \frac{(n-1)d_{p2p}}{v_{trvl}}, \quad [3]$$

and

$$v_{eff} = \frac{(n-1)d_{p2p}}{t_{tot}}, \quad [4]$$

where $t_{tot}$ is the total laser travel time, $n$ is an arbitrary large number of pulses, $t_{exp}$ the length of exposure time of each pulse (80 $\mu$s), $t_{set}$ the settling time of the laser (2 $\mu$s), $d_{p2p}$ the distance traveled by the laser between each pulse (60 $\mu$m), $v_{trvl}$ the speed at which the laser travels between pulses (5 m/s), and $v_{eff}$ the effective travel speed of the pulsed laser. Using this method, the effective laser speed in the Renishaw 250AM was calculated to be 0.638 m/s for the process parameters shown in Table I. Modifying Eq. [2] to produce the pulsed laser, surface-only Rosenthal solution results in the following equation:

$$T(x, R) = T_0 + \frac{P_{abs}}{2\pi\lambda}\left(\frac{1}{R}\right)\exp\left\{-\frac{v_{eff}}{2a}(R+x))\right\}, R = \sqrt{x^2 + y^2} \quad [5]$$

The thermal histories of four points, located 0, 37.5, 75, and 125 $\mu$m from the melt pool edge, respectively, are presented in Figure 13. The 75 and 125 $\mu$m distances were chosen because they represent the halfway points of the 150 and 250 channels built during the HAZ experiments. The halfway points of the channels are assumed to be the points that are least affected by the thermal cycle of the passing laser. The 37.5 $\mu$m distance was chosen to represent a point close to the fusion zone.

As a conservative comparison to the oxide shell thicknesses calculated in Section IV–B–1, the Rosenthal-calculated thermal history for a point positioned at the furthest possible distance (75 $\mu$m) from the edge of the melt pool was input into DICTRA and the spinel (Fe₃O₄) oxide growth as a function of time was

calculated. The thermal history of the powder bed, which was assigned an effective thermal conductivity of 0.2 W/mK, was used as a further method of conservative estimation. A higher value of powder bed thermal conductivity allows heat to dissipate faster and decreases the amount of time that a point within the powder bed experiences elevated temperatures. An initial oxide thickness of 9.036 nm was assumed and only the part of the Rosenthal-calculated thermal history that lies above 500 °C was used as input in the DICTRA calculation. Details of the DCM macro files used to run the DICTRA calculation are given in Appendix D.

The DICTRA-calculated oxide thickness (external growth) value of ~67 nm (Figure 14) greatly exceeds that of the 9-15 nm shell back calculated from measured oxygen pickup data (Section IV–B–1). While the absolute oxide depths in the powder could not be determined from the XPS data in Section III–E, the real depth values should be comparable to those reported in Figure 8.[24] In comparison to the DICTRA-calculated oxide thickness, the XPS-measured values of 15 to 22 nm are three times lower than the model prediction. These results indicate that a simple, steady-state heat-transfer solution may not be adequate to predict the oxide growth potential of unmelted powder experiencing thermal cycling during powder bed laser additive manufacturing processes.

## C. Contribution of Spatter Particles

Oxygen-containing spatter from the SLM process was also considered as a contributing factor to the measured oxygen uptake in powder from the HAZ experiments. Two types of spatter have been found to exist during selective laser processing: liquid metal ejected from the weld pool, and unmelted powder sucked up from the surrounding powder bed. Liquid metal is routinely ejected from the weld pool during SLM processing. The spatter material is liquid at the time of its ejection from the weld pool and remains liquid for some time, $\Delta t$, as it is carried by the cover gas before solidifying in-flight and falling back down to the floor of the build chamber. Research by Bidare *et al.* has demonstrated that bed powder near the melt zone is removed *via* gas flow caused by the rapid evaporation of liquid metal in the weld pool during selective laser melting.[25] This kind of spatter is not expected to have experienced the same amount of oxidation as liquid metal spatter that has resolidified. Unpublished data of bulk measurements of spatter particles, collected by the authors, have shown that as a mixture, spatter particle oxygen content can reach at least as high as 0.100 wt pct (compared to virgin powder at 0.033 wt pct). Even at high temperatures, the solubility of oxygen in solid Fe is low (0.003 wt pct) in comparison to its solubility in the molten state (0.23 wt pct).[26] Therefore, it is hypothesized that most oxygen uptake in the ejected particles must occur while in the liquid state. An example of the physical disparity between ejected material and virgin powder can be seen in Figure 15.

A MATLAB model was developed to help visualize the possible oxygen addition to the powder bed by re-introduced, oxygen-rich, spatter particles. For ease of calculation, laser diffractometer measurements of two collected samples of spatter were converted into volume-averaged monodisperse diameters containing the measured 0.100 (± 0.002) wt pct oxygen. Appendix E details the method by which the volume-averaged monodisperse diameters were calculated.

The model incrementally replaces particles of a virtual 1 cubic centimeter, monodisperse powder bed (particle diameters ranging from 30 to 70 $\mu$m) with spatter particles and outputs the total oxygen content of the powder bed in units of weight percent oxygen. Figure 16 shows the relationship between the bulk oxygen content of the hypothetical powder bed as a function of the number of spatter particles (containing 0.100 wt pct oxygen) residing within the bed. A nonrepresentative model of the effect of 200-$\mu$m spatter is also included to conservatively represent larger particle sizes that are sometimes seen in spatter. Both the number and size of oxygen-containing spatter particles can be seen to have an impact on the predicted bulk oxygen content of the simulated powder bed.

From Figure 16, it is seen that replacing 0.505 pct of a powder bed originally composed of virgin powder particles measuring and average 26.77 $\mu$m in diameter with spatter particles 97.8 $\mu$m in diameter and containing 0.100 wt pct oxygen would increase the oxygen content of the bed from its original 0.033 wt pct to the 0.043 wt pct (± 0.002) value measured in the 150-$\mu$m channels of the HAZ experiments.

While 0.505 pct may intuitively seem like a small percentage, it is actually quite large when viewed in terms of the absolute number of spatter particles. For example, 1 cm$^3$ of perfectly packed (~ 74 pct full density) 26.77 $\mu$m diameter monodisperse particles would equal to approximately $5.37 \times 10^7$ particles. 0.505 pct of $5.37 \times 10^7$ equates to $2.71 \times 10^5$ spatter particles, or 5051 ppm within that 1 cm$^3$ powder bed. Oxygen contribution from smaller spatter particles would necessitate even larger numbers to be present in the powder bed in order to match the experimentally observed value of 0.043 wt pct oxygen. These values are unlikely to be seen in actual SLM processes.

To demonstrate how unlikely it is that re-introduction of spatter particles significantly contributed to the measured oxygen content of the HAZ powders, powder distributions of samples taken from the 150-$\mu$m-wide channels in HAZ2 and HAZ3 were measured by laser diffractometry. The powder size distribution results reveal that 100 pct of the HAZ particles measured had diameters smaller than 67.5 $\mu$m, and therefore the presence of any larger spatter particles within the channels is assumed to be precluded (Figure 17) and not a significant source of oxygen. However, it is worth noting that the samples measured by laser diffractometry were not the same samples that were chemically tested. It lies within the realm of reason that some large amount of spatter could have been present in the

**Table V. Stainless Steel 316L Thermophysical Properties and Laser Parameters Used in Rosenthal Model**

| Property | Symbol | Value | Units | Reference |
|---|---|---|---|---|
| Substrate Temperature | $T_0$ | 298 | K | assumed |
| Absorbed Power | $\lambda_{abs}$ | 0.6 | | 27 |
| Thermal Conductivity | $\Lambda$ | 0.05–0.20 | $\frac{W}{K \cdot m}$ | 28 |
| Effective Weld Speed | $v_{eff}$ | 6.38E-01 | $\frac{m}{s}$ | calculated |
| Effective Density | $\rho$ | 4315 | $\frac{kg}{m^3}$ | measured |
| Specific Heat | $C_p$ | 480 | $\frac{J}{kg \cdot K}$ | 21 |
| Thermal Diffusivity | $\alpha$ | $2.41E-9.66 \times 10^{-8}$ | $\frac{m^2}{s}$ | calculated |
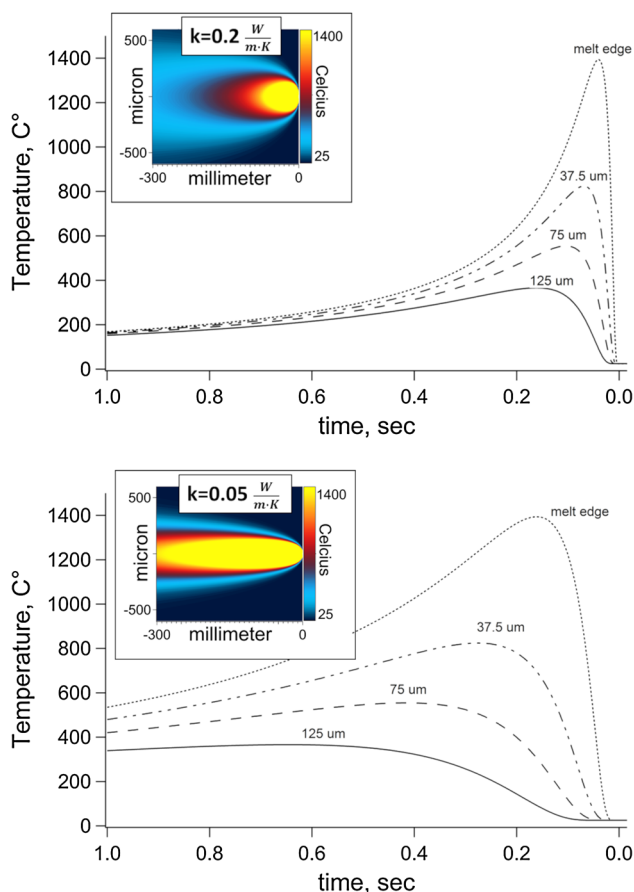


Fig. 13—Thermal history plot of points in the powder bed located 37.5, 75, and 125 microns from the melt pool liquidus. Temperature contour map inset was generated using the Rosenthal equation. Powder bed apparent density = 4315 kg/m³, Heat source velocity = 0.638 m/s, Absorbed Power = (200W*0.6) = 120 W.



Fig. 14—DICTRA calculated $Fe_3O_4$ external oxide growth on the surface of FCC iron as a function of temperature and time.

chemically tested powder samples while remaining absent from the laser diffractometer-measured samples.

Recent observation of the spatter phenomena in the Renishaw AM250 machine was conducted using a high-speed infrared camera. A qualitative review of the amount of spatter that falls back into the powder bed supports the claim that spatter is not likely a significant source of oxygen addition to the powder bed.
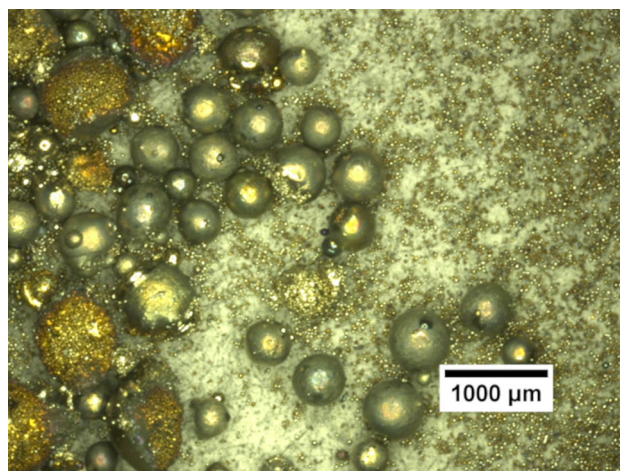


Fig. 15—Optical microscope image of spatter powder mixed with much smaller virgin powder.

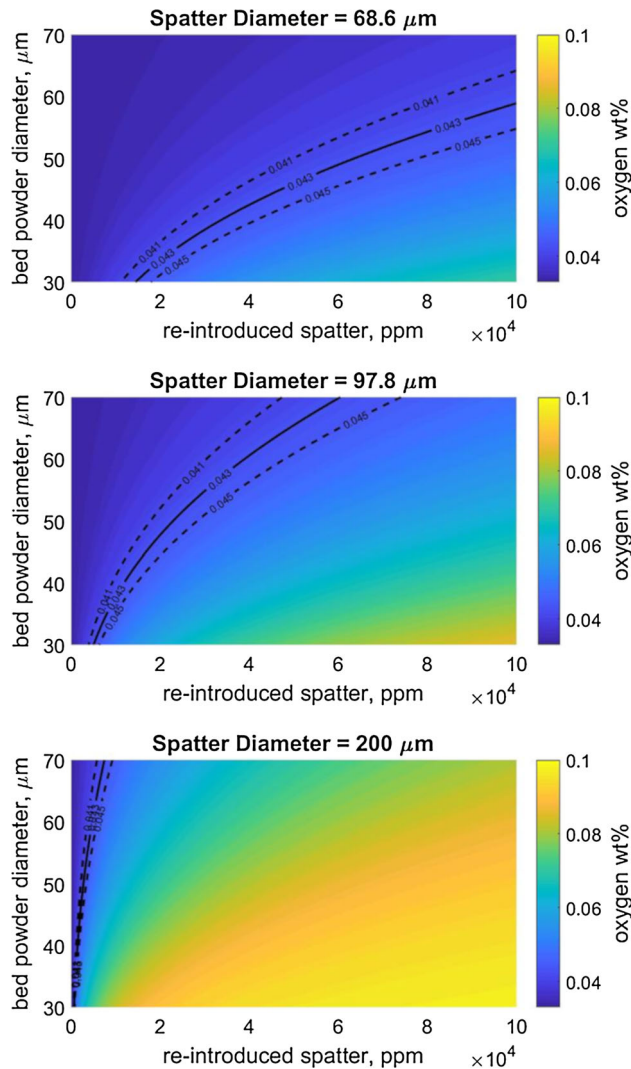Fig. 16—Contour plots modeling the predicated bulk powder bed oxygen content in a monodisperse, oxygen-containing (0.033 ± 0.002 wt pct) powder bed as a function of the addition of 68.6, 97.8, and 200 μm diameter, oxygen-containing (0.100 wt pct) spatter particles, respectively.

## V. MODEL LIMITATIONS

Experimental measurement verification of the predicted oxide layer growth in this study would require TEM sample preparation using the FIB technique of both a virgin powder particle and a particle collected from an area near a melted region. The HAZ experiment powder sample collection method used in this study made it impractical to attempt to find a particle by chance that resided close to the melted region and experienced enhanced oxide growth.

Limited access to appropriate oxide thermodynamic databases limited the DICTRA oxide growth model to a single oxide type ($Fe_3O_4$) grown on a single element (Fe). As mentioned earlier, modification of the thermodynamic and kinetic oxide data is needed to perform more relevant oxide growth calculations under nonisothermal cyclic conditions expected during selective laser melting conditions. Grain boundary effects on oxide growth were not considered in the DICTRA model. Furthermore, the model for oxide formation within DICTRA is not capable of describing the changes from Fe-rich to Cr-rich oxides.

The back calculation of the oxide thicknesses on the processed powder was simplified by assuming single oxide types rather than the complex mix of oxides typically seen in real oxidation of steels. Further simplification of the calculations required a conversion of the real measured powder size distributions into representative, monodisperse powder distributions. The efficacy of the back-calculated estimates is limited by the lack of comparisons to real oxide thickness measurements.

## VI. SUMMARY AND CONCLUSIONS

During the course of this research, it was found that oxygen content in unmelted 316L powder during the SLM process was found to vary as a function of its relative position to the heat source. Measurements of oxygen weight percent in powder samples located very near the melt zone (< 0.25 mm) indicated increased oxygen content. The volume of melted material (i.e., thin vs thick walls) was not found to affect the degree of oxygen pickup in the unmelted powder.

The mechanism driving the oxygen pickup in powder positioned close to melted regions is likely caused by an increase in thickness of the oxide scale on the surface of the unmelted powder particles, promoted by the elevated temperatures and adequate oxygen partial pressure during processing. It was found that dilution effects become considerate even at small length scales (5 mm) and can occlude local changes in powder characteristics (i.e., oxygen pickup) when measuring bulk powder characteristics.

An oxidation model of $Fe_3O_4$ on FCC iron was performed using DICTRA and was found to overestimate the amount of oxidation back calculated from oxygen content and XPS measurements. The DICTRA model used thermal histories calculated by a simple Rosenthal conduction model. The overestimation of oxide thickness predicted by DICTRA may also be in some parts the fault of the Rosenthal model. Access to thermodynamic and kinetic data of oxides is needed to perform more relevant oxidation growth calculations.

The role of spatter and its re-introduction into the powder bed was discussed. It was determined that even though spatter may contain elevated levels of oxygen, it is not likely a significant source of oxygen pickup within the powder bed.

Future studies should include a traditional oxidation study of stainless steel feedstock powder at temperatures and time scales associated with the SLM process. Qualitative examination of the oxide shell both before and after the oxidation studies should be able to validate the conclusions found in this study. Future powder
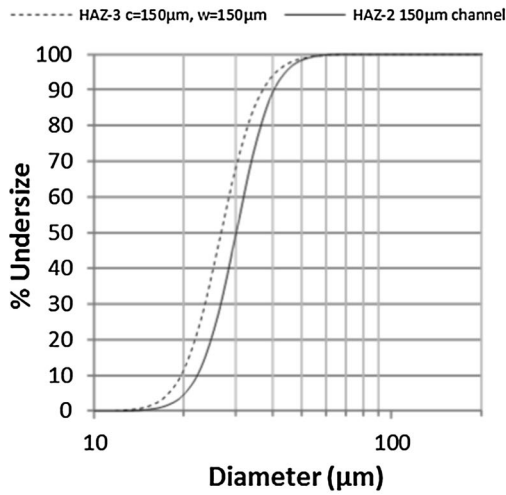
| Diameter (μm) | HAZ 2 Undersize (%) | HAZ 3 Undersize (%) |
|---|---|---|
| 67.523 | 100 | 100 |
| 58.953 | 99.749 | 99.758 |
| 51.471 | 98.811 | 99.118 |
| 44.938 | 95.856 | 97.464 |
| 39.234 | 88.178 | 93.425 |
| 34.255 | 72.274 | 84.449 |
| 29.907 | 49.546 | 68.288 |
| 26.111 | 27.323 | 46.517 |
| 22.797 | 12.123 | 25.573 |
| 19.904 | 4.512 | 11.32 |
| 17.377 | 1.493 | 4.193 |
| 15.172 | 0.454 | 1.376 |
| 13.246 | 0.114 | 0.413 |
| 11.565 | 0 | 0.102 |
| 10.097 | 0 | 0 |

Fig. 17—Laser diffraction percent undersize results from the 150-μm channel in HAZ 2 and the 150-μm channel in HAZ 3 showing what percentage of powder particles are smaller than the corresponding diameter. c: channel width, w: wall thickness.

recyclability studies should be aware of and take into account the localized oxidation in the unmelted powder close to melted regions.

## APPENDIX A: BUILD PARAMETERS

| Scan Strategy: Meander | |
|---|---|
| Hull and Core Overlap | 0.4 mm |
| Wire Structure Shape: Minimal Segment Length | 0.2 mm |
| Layer Path Organization | inside to outside |

| | Volume Area | Volume of Offset Hatch | Volume Border |
|---|---|---|---|
| Power Output (W) | 200 | 180 | 175 |
| Focus Offset (mm) | 0 | 0 | 0 |
| Point Distance (μm) | 60 | 65 | 25 |
| Exposure Time (μs) | 80 | 110 | 130 |

| | Overhang Border | Skin Area | Wire Structure |
|---|---|---|---|
| Power Output (W) | 50 | 125 | 0 |
| Focus Offset (mm) | 0 | 0 | 0.2 |
| Point Distance (μm) | 25 | 65 | 200 |
| Exposure Time (μs) | 65 | 60 | 400 |

| Contour | |
|---|---|
| Layer Spot Composition | 45 $\mu$m |
| Edge Factor | 1.2 |
| Following Distances | 200 $\mu$m |
| Offset Hatch General Offset Number | 1 |
| Offset Hatch General Offset Space | 50 $\mu$m |
| Volume Area | |
| Angle | 0 deg |
| Angle Increment | 67 deg |
| Hatch Space | 110 $\mu$m |
| Contour Space | 100 $\mu$m |
| Skin Area | |
| Angle | 0 deg |
| Angle Increment | 0 deg |
| Hatch Space | 175 $\mu$m |
| Contour Space | 100 $\mu$m |

## APPENDIX B: OXIDE SCALE THICKNESS CALCULATIONS

Appendix B describes the methodology used to arrive at estimated initial and heat-affected-zone oxide thicknesses on a representative powder bed particle. A schematic of a representative steel particle encased in an oxide shell is provided in Figure B1.

To back calculate the initial $Fe_3O_4$ oxide thickness on an average particle, the following variables must be known: the measured oxygen content of the virgin powder (wt pct$_O$ = 0.033 $\pm$ 0.002 wt pct), the density of 316L steel ($\rho_{316L}$ = 7.99 g/cm$^3$), the density of the oxide ($\rho_{Fe_3O_4}$ = 5.17 g/cm$^3$), the stoichiometry of Fe and O within the oxide ($s_{Fe}$ = 3, $s_O$ = 4), the molar mass of Fe and O (MM$_{Fe}$ = 55.845 g/mol, MM$_O$ = 15.999 g/mol), the molar mass of the oxide (MM$_{Fe_3O_4}$ = 231.533 g/mol), and Avogadro's Number ($N_A$ = 6.022 $\times$ 10$^{23}$



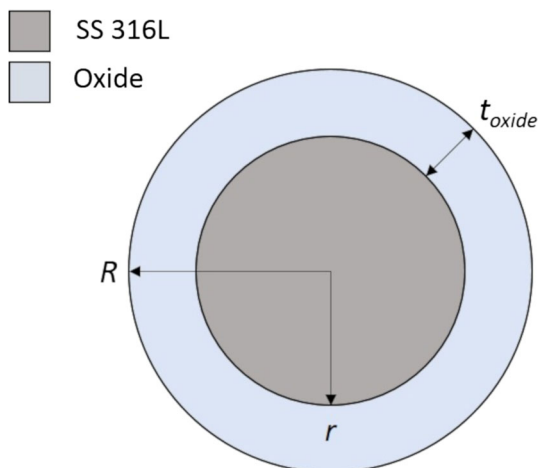Fig. B1—Schematic showing the oxide shell surrounding a stainless steel powder particle.

mol$^{-1}$). It follows that the wt pct of the oxygen within the oxide shell can be determined by equations

$$\text{wt pct}_O = 100 \cdot \frac{m_O}{m_p + m_O} \qquad [B1]$$

$$m_p = \rho_{316L} * V_p \qquad [B2]$$

$$V_p = \frac{\pi}{6}(r)^3 \qquad [B3]$$

where $m_O$ is the mass of the oxygen contained in the oxide layer, $m_p$ is the mass of a single powder particle with no oxide layer, $V_p$ is the volume of a single powder particle with no oxide layer, and $r$ is the radius of a single powder particle with no oxide layer. The virgin powder size distribution (see Section III–D) was used to calculate an average particle radius, $r = D_V/2$, based on the average particle volume ($D_V$ = 27.71 $\mu$m). It is assumed that the Fe needed to form the oxide is supplied by the base material and is therefore included in $m_p$ value of Eq. [B1]. The mass of the oxygen within the initial oxide layer, $m_O$, can be determined by the equations

$$m_O = \frac{m_{oxide} N_A s_O MM_O}{MM_{oxide} N_A} \qquad [B4]$$

$$m_{Oxide} = V_{oxide} * \rho_{Fe_3O_4} \qquad [B5]$$

$$V_{Oxide} = \frac{4\pi}{3}\left((r + t_{Oxide})^3 - r^3\right), \qquad [B6]$$

where $m_{oxide}$ is the mass of the oxide layer, $V_{oxide}$ is the volume of the oxide layer, and $t_{oxide}$ is the thickness of the oxide layer. Since the oxygen content in wt pct is known, it is possible to back calculate using Eqs. [B1] through [B6] to determine the initial oxide thickness, $t_{oxide}$, which will achieve the initial measured wt pct value of 0.033 ($\pm$ 0.002). Microsoft Excel's Goal Seek function works well for this task.

It is a simple matter to repeat the calculations above to find the average oxide thicknesses in the HAZ powder after being thermally cycled, using this time the oxygen content value of 0.043 ($\pm$ 0.002) wt pct, measured from the powder contained in the 150-$\mu$m channels of the HAZ experiments.

## APPENDIX C: POWDER BED DILUTION CALCULATIONS

To calculate the dilution effects of an ever-increasing ratio of non-oxidized powder to oxidized powder, it was assumed that all of the measured oxygen pickup is evenly distributed between the powder particles residing within a 150-$\mu$m-wide channel, which is the narrowest channel in the heat-affected-zone experiments. For simplification purposes, a powder particle diameter ($D_V$) of 30 $\mu$m is assigned to all particles residing within the 150-$\mu$m channel. Furthermore, it is assumed that the
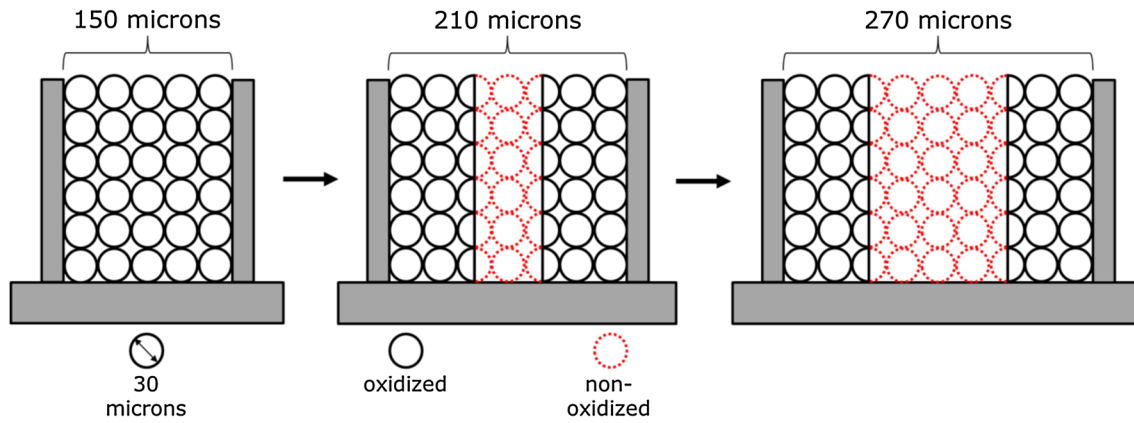
Fig. C1—Schematic demonstrating the diluting effect of non-oxidized powder on locally oxidized powder as channel width is increased.

powder particles are arranged in rows of stacked columns as shown in Figure C1. The oxygen content measured in the heat-affected powder sampled from the 150-$\mu$m channels (wt pct$_{HAZ}$) is 0.043 ($+$ 0.002) wt pct and is represented by solid black outlines in the figure. Diluting powder is assumed to contain the measured oxygen content of the virgin powder (wt pct$_{virgin}$ = 0.033 $+$ 0.002 wt pct) and is represented by red dashed outlines.

As the channel width is increased from 150 microns and more unoxidized powder is added to fill the space between the channel walls, the total oxygen content wt pct of the powder within the channel ($wt\,pct_{bed}$) begins to decrease as described by Eqs. [C1] through [C3].

$$wt\,pct_{bed} = \frac{m_O}{m_{bed}} \qquad [C1]$$

$$m_O = V_p \rho_{316L}(N_{HAZ}wt\,pct_{HAZ} + N_{virgin}wt\,pct_{virgin}) \qquad [C2]$$

$$m_{bed} = V_p \rho_{316L}(N_{HAZ} + N_{virgin}) \qquad [C3]$$

where $m_O$ is the mass of oxygen in powder within the channel, $m_{bed}$ is the total mass of the powder within the channel, $V_p$ is the volume of a powder particle with diameter $D_V$, $\rho_{316L}$ is the density of stainless steel 316L (7.99 g/cm$^3$), $N_{HAZ}$ is the number of powder particles within the heat-affected zone of the channel (black outlines), and $N_{virgin}$ is the number of non-heat-affected powder particles within the channel (red, dashed outlines). $N_{HAZ}$ and $N_{virgin}$ can be determined by assuming any arbitrary height and length for the channel walls and calculating the number of powder particles of diameter $D_V$, arranged in the above geometry, which would fit between them. $N_{HAZ}$ is the number of those particles that reside within 75 microns
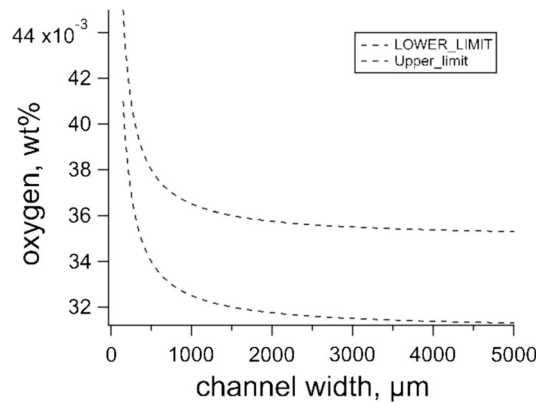


Fig. C2—Plot of the bounded area of the dissolution effect as a function of channel width.

of either channel wall. The remaining particles after subtracting out $N_{HAZ}$ from the total particles are $N_{virgin}$. By performing the above calculations using several increasing channel widths, as well as the upper and lower error bounds of the virgin powder oxygen content (0.035 and 0.031 wt pct) and the upper and lower bounds of the HAZ powder oxygen content (0.045 and 0.041 wt pct), a bounding area of oxygen wt pct as a function of channel width can be produced as shown in Figure C2.

### APPENDIX D: DICTRA MACROS

This Appendix contains the text form of the DCM macro files used to (1) set up the DICTRA calculation, (2) Run the DICTRA calculation, and (3) Plot the thermal history and oxide thickness as functions of time on two separate plots. ThermoCalc version 2017b was used to perform the following calculations.

@@ 05/25/2017
@@ Daniel Galicki
@@ Diffusion in complex phases.
@@ Oxidation of FCC iron sample and consequent growth of an oxide layer.

@@ fcc_oxidation.DCM
@@ WE START BY GOING TO THE DATABASE MODULE
goto-module
database-retrieval

@@ WE SELECT A USER DATABASE FOR READING THE THERMODYNAMIC DATA
switch-database
TCFE8
define-system fe o
reject species *
restore species fe fe+2 fe+3 o o2 o-2 va
reject phases *
restore phases gas fcc spinel
get-data

@@ SWITCH TO A MOBILITY DATABASE TO RETRIEVE MOBILITY DATA FOR FCC
PHASE
append-database
MOBFE3
define-system fe o
reject species *
restore species fe o o2 va
reject phases *
restore phases FCC_A1
get-data

@@ SWITCH TO A USER DEFINED MOBILITY DATABASE TO RETRIEVE MOBILITY
DATA
append-database
user FeOmob.TDB
define-system fe o
reject species *
restore species fe fe+2 fe+3 o o2 o-2 va

reject phases BCC_A2
get-data

@@ ENTER THE DICTRA MONITOR
goto-module
dictra-monitor

@@ ENTER GLOBAL CONDITION TEMPERATURE
set-condition
global
T
0

775.29+(3529.04*TIME)+(-76661.26*(TIME**2))+(602228.84*(TIME**3))+(-
1857433.07*(TIME**4));
*
N
@@ SET REFERENCE STATE FOR O TO O2 (GAS)
set-reference-state
o
gas
323
100000

@@ ENTER REGIONS gam AND sp
enter-region
gam
enter-region
sp
gam
yes

@@ ENTER PHASES INTO REGIONS
enter-phase-in-region
active
gam
matrix
fcc
enter-phase-in-region
active
sp
matrix
spinel

@@ ENTER GRIDS INTO THE REGIONS
@@ Enter a size for the austenite
enter-grid-coordinates
gam
4.99999e-3
linear
50

@@ Enter a thin initial size for the oxide
enter-grid-coordinates
sp
9.036e-9
linear
50

@@ ENTER INITIAL COMPOSITIONS IN FCC
enter-compositions
gam
fcc
mole-fraction
o
linear
1e-9
1e-9

@@ ENTER INITIAL COMPOSITIONS IN THE OXIDE
enter-compositions
sp
spinel
mole-fraction
fe

linear
4.28771e-01
4.28549e-01
@@ ENTER A BOUNDARY CONDITION "GAS" ON THE UPPER (RIGHTMOST) INTERFACE
@@ OF THE OXIDE. THIS WILL ALLOW THE SYSTEM TO EXPAND AND THE OXIDE LAYER
@@ TO GROW EXTERNALY. FOR THIS EXAMPLE WE HAVE SPECIFIED AN OXYGEN ACTIVITY
@@ THAT IS LOW ENOUGH IN ORDER NOT TO FORM CORUNDUM (FE2O3). WE ALSO
@@ SPECIFY THAT THERE IS NO FLUX OF FE ACROSS THIS INTERFACE, I.E. NO FE
@@ IS ALLOWED TO ENTER OR LEAVE THE SYSTEM.
set-condition
boundary
upper
gas-interface
zero-flux
activity
0
8.0947E-8;
*
N

@@ ENTER START VALUES FOR INITIAL INTERFACE VELOCITIE
set-all-start-values
-1e-5
1e-5
yes

@@ SIMULATE FOR 24 HOURS
set-simulation-time
0.104017526004381
yes
0.01040175260
1e-07
1e-07

@@ SPECIFY THAT POTENTIALS AND NOT ACTIVITIES ARE VARIED AT THE PHASE
@@ INTERFACE, AND ALSO USE A FULLY IMPLICIT SCHEME FOR TIME INTEGRATION.
set-simulation-condition
0
1
1
yes
potentials
yes
yes
1
2
no
yes
no

@@ SAVE THE SETUP ON A NEW STORE FILE AND EXIT
save 0.2WmK_75um_tempfunc_fcc_oxidation_500C_acr(O)=8.0947e-8_9.036nm.DIC Y
set-interactive

```
@@ Daniel Galicki
@@ 05/25/2017

@@ fcc_oxidation.DCM
@@ FILE FOR RUNNING fcc_oxidation

@@ ENTER THE DICTRA MONITOR AND READ THE STORE RESULT FILE
@@
goto-module dictra-monitor
read fcc_oxidation

@@ Start the simulation
simulate y
set-interactive
```

```
@@ Daniel Galicki
@@ 05/25/2017

@@ fcc_oxidation.DCM
@@ FILE FOR GENERATING GRAPHICAL OUTPUT FOR fcc_oxidation

@@ GO TO THE DICTRA MONITOR AND READ THE STORE RESULT FILE
goto-module
dictra-monitor
read-workspaces
fcc_oxidation

@@ ENTER THE POST PROCESSOR
post-processor

@@ LET'S PLOT THE THERMAL CYCLE THAT WE ENTERED
set-plot-condition
interface
sp
upper
set-diagram-axis
x
time
set-diagram-axis
y
temperature-celsius
plot-diagram

@@ SELECT A NEW PLOT WINDOW
select-plot
new

@@ LET'S PLOT THICKNESS OF THE OXIDE LAYER GROWING AT THE SURFACE.
@@ FOR THIS PURPOSE, WE NEED TO ENTER A FUNCTION ACCORDING TO
BELOW.
enter-symbol
function
oxideth
poi(sp,upper)-poi(sp,lower);

@@ WE PUT THIS FUNCTION ON Y-AXIS
set-diagram-axis
y
oxideth
plot-diagram
set-interactive
exit
```

# APPENDIX E: CONVERSION OF LASER DIFFRACTION MEASUREMENTS INTO A REPRESENTATIVE, VOLUME-AVERAGED, MONODISPERSE PARTICLE DIAMETER

This appendix describes in detail the calculations used to convert typical laser diffraction measurements of a powder sample into a more easily workable, single, particle diameter value representing every particle in the measured powder sample. An example of laser diffraction measurement values is provided in Figure 17. The "Diameter" and "Undersized" headings in Figure 17 are represented in the following equations by $D_p^i$ and $V_I^i$, respectively.

Equations [E1] through [E4] were used to convert the laser diffraction incremental volume-percent value ($V_I^i$) into an incremental number-percent value ($N_I^i$).

$$V_p^i = \frac{4\pi}{3}\left(\frac{D_p^i}{2*(10,000)}\right)^3 \qquad [E1]$$

$$N_p^i = \frac{V_{hyp} * V_I^i}{V_p^i} \qquad [E2]$$

$$N_p^T = \sum_{i=1}^{m} N_p^i \qquad [E3]$$

$$N_I^i = \frac{N_p^i}{N_p^T}, \qquad [E4]$$

where $V_p^i$ is the volume of a single spherical particle with diameter $D_p^i$, $N_p^i$ is the number of particles with diameter $D_p^i$ residing within a hypothetical measured sample volume ($V_{hyp}$), $N_p^T$ is the sum total number of particles within the hypothetical sample, and $m$ is the number of particle size bins output by the laser diffractometer. In Figure 17, $m$ is equal to 15, for example. For any size sample of powder particles ($n_{sample}$), the volume ($V_f^i$) of the sample contributed by the number fraction of particles with diameter $D_p^i$ can be calculated using Eq. [E5].

$$V_f^i = V_p^i * \left(n_{sample} * N_I^i\right) \qquad [E5]$$

The monodisperse, volume-averaged, particle diameter ($D_{mon}$) of a laser diffractometer-measured powder sample can be calculated using Eq. [E6].

$$D_{mon} = 2 * \frac{3}{4\pi}\left[\left(\left(\frac{\sum_{i=1}^{m} V_f^i}{n_{sample}}\right)^{1/3}\right) * 10,000\right] \qquad [E6]$$

The above equations were used in this paper to convert laser diffraction measurements for virgin powder and spatter samples. Table E1 contains data from the measurement of one such spatter sample, and the

**Table E1. Example of Calculation of Monodisperse, Volume-Averaged Particle Diameter from Laser Diffractometer-Measured Data**

| $i$ | $n_{sample}$ 1,000,000 $V_{hyp}$ 1 $D_p^i$ | $V_I^i$ | $V_p^i$ | $N_p^i$ | $N_I^i$ (Pct) | $r_{mon}$ 31.13 $D_{mon}$ 62.26 $n_{sample} * N_I^i$ | $V_f^i$ |
|---|---|---|---|---|---|---|---|
| 1 | 344.21 | 0.307 | 2.14E-05 | 1.44E+04 | 0.0018 | 18.17 | 3.88E-04 |
| 2 | 300.52 | 0.552 | 1.42E-05 | 3.88E+04 | 0.0049 | 49.09 | 6.98E-04 |
| 3 | 262.38 | 0.993 | 9.46E-06 | 1.05E+05 | 0.0133 | 132.69 | 1.25E-03 |
| 4 | 229.08 | 1.847 | 6.29E-06 | 2.93E+05 | 0.0371 | 370.85 | 2.33E-03 |
| 5 | 200.00 | 3.209 | 4.19E-06 | 7.66E+05 | 0.0968 | 968.15 | 4.06E-03 |
| 6 | 174.62 | 5.219 | 2.79E-06 | 1.87E+06 | 0.2366 | 2,365.92 | 6.60E-03 |
| 7 | 152.45 | 7.928 | 1.86E-06 | 4.27E+06 | 0.5400 | 5,400.33 | 1.00E-02 |
| 8 | 133.10 | 11.011 | 1.23E-06 | 8.92E+06 | 1.1270 | 11,270.11 | 1.39E-02 |
| 9 | 116.21 | 13.585 | 8.22E-07 | 1.65E+07 | 2.0893 | 20,892.67 | 1.72E-02 |
| 10 | 101.46 | 14.629 | 5.47E-07 | 2.68E+07 | 3.3806 | 33,806.09 | 1.85E-02 |
| 11 | 88.58 | 12.240 | 3.64E-07 | 3.36E+07 | 4.2501 | 42,500.61 | 1.55E-02 |
| 12 | 77.34 | 8.738 | 2.42E-07 | 3.61E+07 | 4.5589 | 45,589.45 | 1.10E-02 |
| 13 | 67.52 | 5.976 | 1.61E-07 | 3.71E+07 | 4.6851 | 46,851.15 | 7.55E-03 |
| 14 | 58.95 | 4.083 | 1.07E-07 | 3.81E+07 | 4.8098 | 48,097.94 | 5.16E-03 |
| 15 | 51.47 | 2.768 | 7.14E-08 | 3.88E+07 | 4.8994 | 48,994.03 | 3.50E-03 |
| 16 | 44.94 | 1.928 | 4.75E-08 | 4.06E+07 | 5.1278 | 51,277.95 | 2.44E-03 |
| 17 | 39.23 | 1.402 | 3.16E-08 | 4.43E+07 | 5.6031 | 56,030.58 | 1.77E-03 |
| 18 | 34.26 | 1.076 | 2.10E-08 | 5.11E+07 | 6.4611 | 64,610.81 | 1.36E-03 |
| 19 | 29.91 | 0.827 | 1.40E-08 | 5.90E+07 | 7.4619 | 74,619.41 | 1.05E-03 |
| 20 | 26.11 | 0.616 | 9.32E-09 | 6.61E+07 | 8.3517 | 83,517.03 | 7.78E-04 |
| 21 | 22.80 | 0.439 | 6.20E-09 | 7.08E+07 | 8.9433 | 89,432.69 | 5.55E-04 |
| 22 | 19.90 | 0.300 | 4.13E-09 | 7.27E+07 | 9.1826 | 91,825.86 | 3.79E-04 |
| 23 | 17.38 | 0.199 | 2.75E-09 | 7.24E+07 | 9.1536 | 91,536.34 | 2.51E-04 |
| 24 | 15.17 | 0.130 | 1.83E-09 | 7.11E+07 | 8.9842 | 89,842.06 | 1.64E-04 |
| | | | | $N_p^T$ 7.91E+08 | | 1,000,000 | |

values obtained from the application of Eqs. [E1] through [E6].

## REFERENCES

1. Z. Sun, X. Tan, S. Tor, and W. Yong: *JMADE*, 2016, vol. 104, pp. 97–204.
2. B. Almangour, D. Grzesiak, T. Borkar, and J. Yang: *Mater. Des.*, 2018, vol. 138, pp. 119–28.
3. I. Yadroitsev, P. Krakhmalev, I. Yadroitsava, S. Johansson, and I. Smurov: *J. Mater. Process. Tech.*, 2013, vol. 213, pp. 606–13.
4. H.P. Tang, M. Qian, N. Liu, X.Z. Zhang, G.Y. Yang, and J. Wang: *JOM*, 2015, vol. 67, pp. 555–63.
5. P. Nandwana, W.H. Peter, R.R. Dehoff, L.E. Lowe, M.M. Kirka, F. Medina, and S.S. Babu: *Metall. Mater. Trans. B*, 2015, vol. 47B, pp. 754–62.
6. Y. Liu, Y. Yang, S. Mai, D. Wang, and C. Song: *Mater. Des.*, 2015, vol. 87, pp. 797–06.
7. Renishaw plc: White Paper, Renishaw, Staffordshire, 2016.
8. DoITPoMS, The Ellingham Diagram. (University of Cambridge, 2018), https://www.doitpoms.ac.uk/tlplib/ellingham_diagrams/ellingham.php. Acessed 01 Jan 2016.
9. N. Birks, G.H. Meier, and F.S. Pettit: *Introduction to the High-Temperature Oxidation of Metals*, 2nd ed., Cambridge University Press, New York, 2006.
10. E. Fromm: *Kinetics of Metal-Gas Interactions at Low Temperatures*, Springer, Berlin, 1998.
11. R. Guillamet, J. Lopitauz, B. Hannoyer, and M. Lenglet: *Le J. Phys.*, 1993, vol. 3, pp. 349–56.
12. K.A. Habib, M.S. Damra, J.J. Saura, I. Cervera, and J. Bellés: *Int. J. Corros.*, 2011, vol. 2011, pp. 1–10.
13. M.F. McGuire: *Stainless Steels for Design Engineers*, Ohio, ASM International, 2008, pp. 57–68.
14. J. Tarabay and V. Peres: *M. Pijolat.*, 2013, vol. 80, pp. 311–22, https://doi.org/10.1007/s11085-013-9387-x.
15. T. Debroy and S.A. David: *Rev. Mod. Phys.*, 1995, vol. 67, pp. 85–112.
16. T. Hibiya and S. Ozawa: *Cryst. Res. Technol.*, 2013, vol. 48, pp. 208–13.
17. E. Louvis, P. Fox, and C.J. Sutcliffe: *J. Mater. Process. Technol.*, 2011, vol. 2311, pp. 275–84.
18. Bruker AXS GmbH, D2 Phaser 2nd Generation, https://www.bruker.com/fileadmin/user_upload/8-PDF-Docs/X-rayDiffraction_ElementalAnalysis/XRD/Brochures/D2_PHASER_2ndGen_Brochure_DOC-B88-EXS017-V2_web.pdf. Accessed 13 Sept 2015.
19. Bruker AXS GmbH, Spec Sheet XRD 27 LYNXEYE-Super Speed Detector for X-ray Powder Diffraction. https://www.bruker.com/fileadmin/user_upload/8-PDF-Docs/X-rayDiffraction_ElementalAnalysis/XRD/ProductSheets/LYNXEYE_DOC-S88-EXS027_V4_high.pdf. Accessed 13 Sept 2015.
20. ASTM E1019: *ASTM Int.*, 2003, vol. 03, pp. 1–28.
21. C. Oikonomou, D. Nikas, E. Hryha, and L. Nyborg: *Surf. Interface Anal.*, 2014, vol. 46, pp. 1028–32.
22. B. Almangour, D. Grzesiak, J. Cheng, and Y. Ertas: *J. Mater. Process. Tech.*, 2018, vol. 257, pp. 288–301.
23. D. Rosenthal: *Trans. Am. Soc. Mech. Eng.*, 1946, vol. 68, pp. 849–66.
24. R.L. Tapping, R.D. Davidson, and T.E. Jackman: *Surf. Interface Anal.*, 1985, vol. 7, pp. 105–08.
25. P. Bidare, I. Bitharas, R.M. Ward, M.M. Attallah, and A.J. Moore: *Acta Mater.*, 2018, vol. 142, pp. 107–20.
26. O. Kubaschewski: *IRON: Binary Phase Diagrams*, 1st ed., Springer, Berlin Heidelberg GmbH, Berlin, 1982, pp. 79–82.
27. C.D. Boley, S.A. Khairallah, and A.M. Rubenchik: *Appl. Opt.*, 2015, vol. 54, pp. 2477–82.
28. M.R. Alkahari, T. Furumoto, T. Ueda, A. Hosokawa, R. Tanaka, and MSA. Aziz: *Key Eng. Mater.*, 2012, vols. 523–524, pp. 244–49.